Polymer 311 (2024) 127562

Contents lists available at ScienceDirect

Polymer

journal homepage: www.elsevier.com/locate/polymer

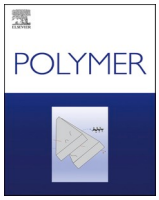

Decoding the interplay of mold temperature and catalysts concentration on the crystallinity and mechanical properties of anionic polyamide 6: a combined experimental and statistical approach

Giulia Fredi *, Lorenzo Broggio, Martino Valentini, Mauro Bortolotti, Daniele Rigotti, Andrea Dorigato, Alessandro Pegoretti

University of Trento, Department of Industrial Engineering and INSTM Research Unit, Via Sommarive 9, 38123, Trento, Italy

ARTICLE INFO

Keywords:
Reactive thermoplastics
Polyamide 6
Response surface method
Mechanical properties
Thermal properties
Crystallinity

ABSTRACT

Anionic polyamide 6 (aPA6), synthesized via the ring-opening polymerization of ε-caprolactam, has emerged as a promising matrix for high-performance thermoplastic composites, offering advantages over conventional thermoplastics and thermosets. However, optimizing the microstructure and mechanical properties of aPA6 requires a comprehensive understanding of how processing conditions influence polymerization kinetics and resulting material characteristics. This work systematically investigates the interplay between two critical processing parameters, i.e., the mold temperature and catalysts concentration, on the microstructural and thermo-mechanical properties of aPA6, via a combined experimental and statistical approach. Increasing the mold temperature from 145 °C to 175 °C and the catalysts concentration led to a reduction in crystallinity, due to the promotion of polymerization over crystallization. Higher temperatures and concentrations also slightly anticipated thermal degradation onset from 388 °C to 327 °C. The elastic modulus decreased from 3.4 GPa to 2.7 GPa as temperature increased, primarily governed by the diminishing crystallinity. Similarly, the ultimate tensile strength declined from 80 MPa to 68 MPa with rising temperature. Interestingly, the strain at break exhibited a complex dependence, peaking at 48 % for an intermediate temperature of 165 °C and lower catalysts concentration, suggesting an optimal balance of crystallinity, branching, and high molecular weight. Statistical empirical models captured these relationships, enabling prediction and tailoring of aPA6 properties by tuning processing conditions. These insights pave the way for optimized manufacturing of high-performance aPA6 composites via techniques like thermoplastic resin transfer molding and expand potential applications to thermally sensitive reinforcements like natural fibers.

1. Introduction

Reactive thermoplastics have gained significant attention in the composite industry owing to their distinct advantages over traditional thermoplastic and thermosetting matrices [1,2]. In these systems, a melted monomer is combined with the polymerization catalysts and then transferred into a mold where polymerization occurs. The low viscosity of the reactive mixture allows it to easily infiltrate dry reinforcements, thereby solving the primary issue associated with thermoplastic matrices in composite production. Compared to traditional thermoplastics, reactive thermoplastics also offer faster processing times, the ability to produce near-net-shape components, and the potential for enhanced filler/matrix interfacial interaction by grafting polymerization catalysts directly onto the reinforcement surface [3,4]. Reactive thermoplastics also offer advantages over traditional thermosetting matrices. Unlike thermosets, which undergo irreversible cross-linking during curing, reactive thermoplastics can be reprocessed, post-thermoformed, and recycled, thus offering greater flexibility and reducing waste in manufacturing processes. Also, they typically exhibit superior impact resistance, toughness, and damage tolerance compared to thermosets, making them well-suited for demanding structural applications [5–7].

Among reactive thermoplastics, anionic polyamide 6 (PA6) has emerged as a promising matrix material for high-performance composites [8]. The interest in PA6 for composites has been steadily growing, driven by its excellent mechanical properties, chemical resistance, and

* Corresponding author.
E-mail address: giulia.fredi@unitn.it (G. Fredi).

https://doi.org/10.1016/j.polymer.2024.127562
Received 9 June 2024; Received in revised form 26 August 2024; Accepted 29 August 2024
Available online 30 August 2024

thermal stability. The ability to synthesize PA6 via byproduct-free, anionic ring-opening polymerization (aROP) of ε-caprolactam (ε-CL) offers the aforementioned advantages over conventional melt processing techniques, as well as the potential for enhanced mechanical properties [9]. The process of anionic polymerization of CL occurs well below the polymer's melting point (~221 °C), which results in a polymer with a low content of low-molar-mass portions and a very high crystallinity degree [10]. The low temperature process could also enable the production of composites with PA6 fibers (single polymer composites, SPCs [11]), as demonstrated in the literature [12–17], as well as with other thermally sensitive reinforcements such as natural fibers. Natural fibers typically require processing below 200 °C and are generally coupled with thermosetting resins or low-melting thermoplastic, such as polyethylene or polypropylene. Hence, aROP of PA6 presents a unique opportunity to produce natural-fiber-reinforced composites with a high-performance thermoplastic matrix, which could expand their application. However, to fully exploit the potential of anionic PA6 (aPA6) composites processed via liquid composite molding (LCM) techniques such as thermoplastic resin transfer molding (*t*-RTM), it is crucial to optimize the properties of the matrix material by systematically investigating the key processing parameters [18,19].

Well known is the reaction of anionic polymerization of PA6, which involves a complex three-step mechanism [10,20]. First, an initiator, typically an alkali metal or organometallic compound, dissociates to form the necessary anionic species that can initiate the polymerization. Next, an activator, such as an acyllactam or organophosphorus compound, forms a complex with the initiator, enhancing the reactivity of the anionic species. Finally, the polymerization occurs through the addition of the monomer units to the growing anion, during which the anion is regenerated with the addition of each new monomer. Such a complex mechanism is inhibited by all proton-donating species, such as moisture [10]. Hence, strict control of the manufacturing environment, with low moisture content (below 200 ppm) and an inert atmosphere, is crucial to ensure the successful anionic polymerization of PA6 and the production of high-quality materials with a high degree of conversion from monomer to polymer [21,22].

The resulting PA6 material, in terms of conversion degree, microstructure, crystallinity, and final mechanical and functional properties, strongly depends on the polymerization conditions [20,23]. Two key parameters that control the reaction are the type and concentration of catalysts (initiator and activator) and the polymerization temperature. The choice and amount of activator and initiator have a significant impact on the polymerization rate and the final microstructural and mechanical properties of PA6. The activator and initiator collaborate in creating the reactive anionic species that initiate the polymerization process. Hence, the specific combination of activator and initiator, as well as their concentrations, determine the rate at which these anionic species are generated and the extent to which they can participate in chain growth. Faster polymerization rates achieved with more reactive activator-initiator combinations or higher concentrations can lead to incomplete conversion and higher levels of residual monomer, which acts as a plasticizer and reduces mechanical properties. Increasing the initiator concentration beyond an optimal level can also decrease the final degree of conversion, as more initiator cations need to be compensated for by unreacted monomer [20]. Conversely, slower polymerization rates, produced by the accurate choice of the initiator-activator chemistry and concentration, allow for greater conversion and more optimal development of the PA6 microstructure, resulting in higher crystallinity and superior mechanical performance, but this could decrease the production rates [24]. Therefore, the selection and optimization of the activator and initiator system is critical for balancing the polymerization kinetics, the final degree of conversion, and the desired final material properties, particularly for manufacturing processes like vacuum infusion where precise control over the reaction rate is essential.

The polymerization temperature has also a significant impact on the polymerization reaction and final properties of aPA6. In general, an increase in polymerization temperature results in a higher polymerization rate, a higher degree of branching, and a lower degree of crystallinity [23,25]. At higher temperatures, the polymerization proceeds more rapidly, leading to a higher conversion in a lower time. However, the increased branching that occurs at elevated temperatures can reduce the final degree of conversion by decreasing the number of reactive chain-end groups [13]. The lower degree of crystallinity observed at higher temperatures is attributed to the reduced tendency of the polymer chains to organize into crystalline regions due to the reduced subcooling, as well as the disruption caused by the increased branching. Above 180 °C, the temperature of the reactive mixture may exceed the melting temperature of PA6 (221 °C), due to the exothermicity of the polymerization and crystallization events, and this results in morphology and properties that resemble those of hydrolytic PA6. Conversely, at excessively low polymerization temperatures (below 130 °C), the rapid crystallization can trap unreacted monomer and reactive chain ends within the crystals, leading to a reduction in overall conversion and the development of voids, both of which degrade the mechanical performance. Hence, the suitable temperature interval for aROP of PA6 is 140–175 °C. These changes in the microstructure of the aPA6 have important implications for the mechanical properties. Young's modulus, tensile strength, chemical resistance, and gas barrier properties increase with the degree of crystallinity, while elongation at break and toughness generally decrease [26].

While previous research has explored the individual effects of polymerization temperature and catalysts concentration on the properties of anionic PA6, a systematic investigation of the interplay between these two critical processing parameters and their impact on the microstructural and thermomechanical performance of the material has not been reported. Such a comprehensive understanding is crucial for optimizing the processing conditions and ensuring the reliable production of high-performance anionic PA6 composites via *t*-RTM techniques.

Hence, the aim of this work is to systematically evaluate the microstructural and thermomechanical properties of anionic PA6 as a function of the mold temperature and the concentration of the catalysts. Through a combined experimental and statistical approach, we aim to identify the key correlations between the processing parameters and the mechanical performance of the anionic PA6 material, providing valuable insights for the optimization of T-RTM processing of this promising thermoplastic composite matrix.

2. Materials and methods

2.1. Materials

ε-caprolactam (ε-CL), with commercial name AP-Nylon® Caprolactam, was used with the initiator Bruggolen C10® (17–19 % sodium caprolactamate in ε-CL) and the activator Bruggolen C20P® (blocked diisocyanate, 17 % NCO content blocked with ε-CL). These three products were kindly provided by Brüggemann GmbH (Heilbronn, Germany) and stored in dry conditions until use. The chemical formula of these products is shown in Fig. 1.

2.2. Sample preparation

The sample preparation route is schematized in Fig. 1 ε-CL was first melted in a three-necked round bottom flask and stirred at 110 °C for 45 min under N_2 flux. C10 was then added in well-defined amounts (see Table 1) and the mixture was then stirred for 30 more minutes N_2 flux. In the end, C20P was added and stirred for 90 s, after which the reactive mixture was transferred, with the pressure of nitrogen gas, in a vertically placed, preheated mold through preheated Teflon tubes. The two employed molds, made of aluminum, were designed to obtain six 1BA dumbbell specimens (standard ISO 527). After the transfer and complete filling of the mold, the reactive mixture was left polymerizing in the

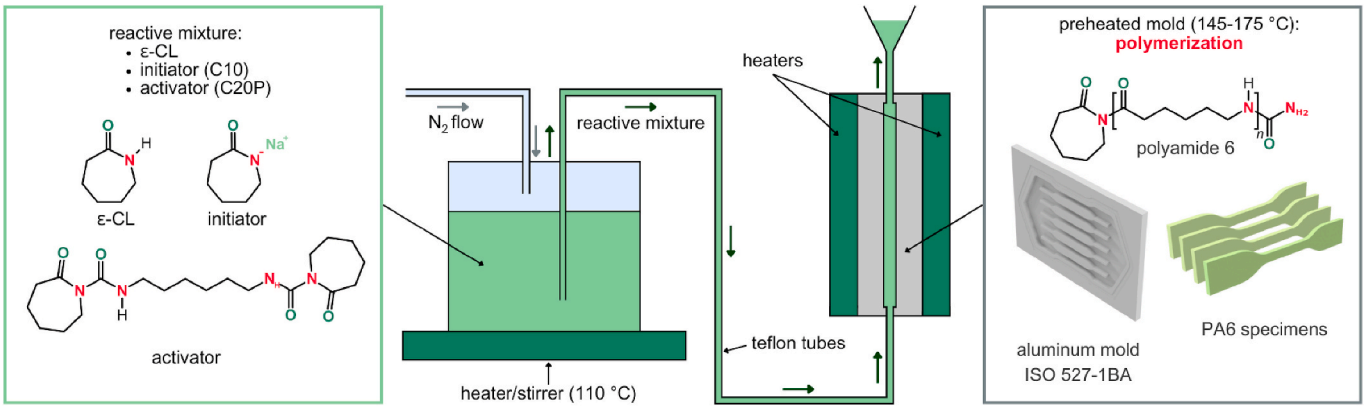

Fig. 1. Schematic of the lab-scale thermoplastic resin transfer molding setup. On the left, the chemical formulas of ε-CL and the active compounds in the initiator C10 (sodium caprolactamate) and the activator C20P (blocked diisocyanate, hexamethylene dicarbamoylcaprolactam) are shown.

Table 1
List of the prepared samples with nominal composition and mold temperature.

Sample	εCL (phr[a])	Initiator (C10) (phr[a])	Activator (C20P) (phr[a])	Mold temperature (°C)
145-L	100	2.20	1.50	145
145-M	100	3.30	2.25	145
145-H	100	4.40	3.00	145
155-L	100	2.20	1.50	155
155-M	100	3.30	2.25	155
155-H	100	4.40	3.00	155
165-L	100	2.20	1.50	165
165-M	100	3.30	2.25	165
165-H	100	4.40	3.00	165
175-L	100	2.20	1.50	175
175-M	100	3.30	2.25	175
175-H	100	4.40	3.00	175

[a] phr = parts per hundred resin, i.e., grams every 100 g of εCL.

mold at well-defined temperatures (see Table 1) for 30 min. Since the demolding time and the post-polymerization heat have been shown to affect the total conversion [27], this time has been kept constant across all the compositions. Then, the mold heaters were switched off and the sample was demolded immediately. The produced specimens were stored in a dry environment (under dry silica gel) until testing.

The optimum concentration of C10 and C20P in ε-CL depends on many factors, such as the dimension and size of the cast parts, processing temperatures, desired reaction time, and target physical properties [24]. In this experimental work, C10/C20P relative ratios were chosen starting from previous research work by our group and data from the literature [20]. In fact, these production parameters allowed the obtainment of a high monomer conversion (>98.5 %), as will be illustrated in the Results and Discussion section.

2.3. Characterization

Density tests were carried out with a helium pycnometer AccuPyc 1330 (Micromeritics Instrument Corporation, Norcross, GA, USA), mounting a chamber of 1 cm^3. 99 consecutive measurements were performed, and the density was evaluated as the average of the last thirty measurements.

Residual ε-CL was evaluated by following the method proposed by Van Rijswijk et al. [23]. Dry specimens of rectangular cross-section and nominal dimensions of 5 × 5 × 2 mm^3 were prepared and weighted (m_{tot}). Subsequently, they were soaked in boiling distilled water for 1 h thanks to a reflux station with a condensation column. The specimens were then left to dry for 100 h at 80 °C in a vacuum oven and then weighed (m_{pol}). The conversion degree (CD_w) [%] was calculated via Eq. (1), as

$$CD_w = \frac{m_{pol}}{m_{tot}} \cdot 100. \quad (1)$$

Differential scanning calorimetry (DSC) was performed via a Mettler DSC 30 (Mettler Toledo Inc., Columbus, Ohio, USA). Specimens with an approximate weight of 10 mg were sealed in aluminum crucibles and subjected to a heating/cooling/heating cycle between 0 °C and 250 °C at ±10 °C/min, under a constant nitrogen flow of 100 ml/min. The tests allowed measuring the melting and crystallization temperatures (T_m and T_c) and enthalpies (ΔH_m and ΔH_c) and calculating the degree of crystallinity (χ) via Eq. (2), as

$$\chi = \frac{\Delta H_m - \Delta H_{cc}}{\Delta H_0} \cdot 100, \quad (2)$$

where ΔH_{cc} is the cold crystallization enthalpy and ΔH_0 is the theoretical melting enthalpy of a 100 % crystalline polymer, equal to 230 J/g for the α form of PA6 [19].

To evaluate the microstructural features and the crystallinity of the prepared samples as a function of the catalysts concentration, X-ray diffraction (XRD) patterns of all L-composition matrices (see Table 1) were acquired. Two-dimensional X-ray diffraction images were acquired with a Unitn Textris diffractometer equipped with a Dectris Eiger 1 M hybrid-pixel detector and a microfocus Cu-anode source operating at 40 kV and 0.9 μA coupled with a 2D multilayer mirror optics. Samples were placed in transmission geometry with a 59.5 mm sample-detector distance. The 2D WAXS images were integrated using the DAWN software [28]. Given the absence of any significant preferred orientation effect, no slicing was performed in the 2D image and the one-dimensional (1D) WAXS profiles were obtained by isotropic azimuthal integration. The sample-detector distance was set to 45 mm. Data acquisition was carried out over the 2θ range 7–50° with a total acquisition time of 100 s per sample. All specimens had a thickness between 0.4 and 1.0 mm. The 1D profiles were further examined to obtain the fraction of the crystalline phase. In a first semi-quantitative approximation, the apparent crystalline phase content was estimated by computing the relative areas under the Bragg reflections and the amorphous region, using Eq. (3),

$$X_C = \frac{A_C}{A_C + A_A}, \quad (3)$$

where A_C and A_A are the area under the crystalline and amorphous features in the pattern, respectively. The areas were estimated by fitting the amorphous background with a cubic spline polynomial through 12 background points and integrating the upper and lower region counts. A more rigorous quantification was tested via full-profile (Rietveld)

fitting, starting from the structural model of the α−form of PA6 as described in Ref. [29]. The structure crystallizes in the P 21 space group, with the asymmetric unit containing 8 monomer units and the chains fully extended in a zig-zag conformation. Quantitative power diffraction analysis was carried out using the ReX software [30], by simulating the amorphous fraction with a second phase with the same crystal structure and crystalline domain sizes set to 1 nm [31]. Phase scale factors, background parameters, lattice constants, and rigid body coordinates of the chain fragments were refined to obtain a satisfactory fit of the experimental profile (Fig. S1).

Thermogravimetric analysis (TGA) was carried out to measure the resistance of the material to thermal degradation. TGA was performed via the IR thermobalance Mettler TG 50 (Mettler Toledo Inc.). Specimens of approx. 10 mg were subjected to a thermal ramp between 30 °C and 700 °C with a heating rate of 10 °C/min, under a constant nitrogen flux of 10 ml/min. This test allowed the determination of the temperatures corresponding to a mass loss of 1 wt%, 3 wt%, and 5 wt% ($T_{1\%}$, $T_{3\%}$, $T_{5\%}$), the onset temperature for degradation using the tangent method (T_{onset}), the mass lost at 250 °C, corresponding to the degradation temperature of residual ε-CL ($m_{L,250}$), the residual mass at 700 °C ($m_{R,700}$), and the degradation temperature (T_d), at the maximum of the first derivative of the TGA thermogram (DTG). A conversion degree according to TGA results (CD_{TGA}) was then calculated as 100-$m_{L,250}$.

Dynamical mechanical thermal analysis (DMTA) was performed to investigate the material response to stress and temperature and to capture the thermal behavior of the prepared PA6 samples around the glass transition. DMTA tests were performed via the DMA Q800 (TA Instruments, Inc., New Castle, DE, USA) in single cantilever mode (span = 17.5 mm), with a strain amplitude of 0.05 % applied at a frequency of 1 Hz. The test was performed on the samples 145-L, 155-L, 165-L, 175-L, 165-M, and 165-H, in the temperature range of 0–150 °C with a heating rate of 3 °C/min. The storage modulus (E'), loss modulus (E''), and loss factor ($tan\ \delta$) were measured as a function of temperature. The glass transition temperature was evaluated at the peak of E'' ($T_{g,E''}$).

Tensile tests were performed under quasi-static conditions with an Instron 5969 (Instron, Norwood, MA, USA) universal electromechanical dynamometer equipped with a 10-kN load cell, according to the standard ISO 527. For the measurement of the elastic modulus (E), five as-produced dumbbell specimens were tested at 0.25 mm/min up to a strain of 0.3 %, and the strain was measured with an Instron 2620 extensometer. The elastic modulus was then calculated as the slope of the segment intercepting the stress-strain curve between the strain levels of 0.05 % and 0.25 %. For the measurement of the properties at break, at least five additional specimens were tested at 1 mm/min until fracture. The test allowed the measurement of the ultimate tensile strength (UTS) as the maximum stress sustained by the specimen during the test, the tensile stress at break (σ_{bf}), and the strain at break (ε_b). The tensile fracture surfaces of two representative compositions, i.e., 145-H and 165-L, were then observed via field emission scanning electron microscopy (FE-SEM). The specimens were placed on a conductive strip over a metallic stub and then subjected to Pt–Pd sputtering. Micrographs were taken at different magnifications with a Zeiss SUPRA 40 FE-SEM (Carl Zeiss Industrielle Messtechnik GmbH, Oberkochen, Germany).

The statistical analysis was carried out with the programming language R, in the environment RStudio [32]. The two considered factors were the mold temperature (T_{mold}) and the mixture composition, i.e., the catalysts' concentration (C). As described in Section 2.2, four levels were considered for the mold temperature (i.e., 145, 155, 165, and 175) and three levels were considered for the composition (i.e., L, M, and H). All the possible combinations of levels of the different factors were considered, for a total of the 12 treatments listed in Table 1. The considered dependent variables (yields) were the mechanical parameters E, UTS, and ε_b.

After checking the normality of the data distribution through Q-Q plots and the Shapiro-Wilk test, a correlation matrix was built via the calculation, for each couple of variables, of the Pearson's r index [33] as reported in Eq. (4),

$$r_{ab} = \frac{\sum_{i=1}^{n}(x_i - \bar{x})(y_i - \bar{y})}{\sqrt{\sum_{i=1}^{n}(x_i - \bar{x})(y_i - \bar{y})}}, \quad (4)$$

where x and y are two of the dependent or independent variables (T_{mold}, C, E, UTS, and ε_b) and $\bar{x}$ and $\bar{y}$ their mean values.

Then, after an outliers analysis, the results were statistically treated via the analysis of variance (ANOVA) method. A two-way ANOVA was performed on the results of E, UTS, and ε_b as a function of the factors T_{mold} and C and the null hypothesis was rejected with p-values smaller than 0.05 (95 % confidence interval). Subsequently, on the factor for which the ANOVA test gave significant results, the post hoc Tukey's honest significant difference (HSD) test was performed to compare the groups and identify which groups were significantly different from one another.

Finally, the results of the mechanical tests were also analyzed with the response surface method (RSM) [34], which allows the obtainment of predictive empirical models for the yields E, UTS, and ε_b. A full quadratic response surface was employed to model the influence of the considered factors on the target mechanical property, with the general formula reported in Eq. (5),

$$Y = c_0 + c_1X_1 + c_2X_2 + c_3X_1X_2 + c_4X_1^2 + c_5X_2^2 \quad (5)$$

where Y is the specific yield, X_1 and X_2 the two considered factors, and c_0 to c_5 are the empirical coefficients. In the model equations, both factors were normalized between −1 and +1, so that the factor effects can be directly compared by comparing the coefficients. For each yield, not all the terms reported in Eq. (5) were included, but only the significant ones from a subsequent ANOVA analysis. Moreover, a lack of fit test was performed on each model to ensure that the polynomial equation with the lowest possible order was employed to fit each yield. Finally, a residual analysis was performed to ensure that the residuals were normally distributed (Q-Q plots and Shapiro-Wilk tests) and did not present any relevant pattern. It is crucial to emphasize that the proposed models are effective only when interpolating within the specified variable range, whereas extrapolation may produce inaccurate outcomes [35].

3. Results and discussion

Fig. 2a shows the DSC thermograms (first heating, cooling, second heating scans) of some selected compositions, namely the samples with composition L. The DSC thermograms of all the other compositions are reported in the Supplementary Materials (Fig. S2). All DSC thermograms reflect the thermal behavior of thermoplastic semicrystalline polymers and are in line with what has been found for other aPA6 samples from the literature [23,36]. The T_g is not clearly detectable and was not extracted from thermograms, although a slight inflection suggests a T_g between 40 and 55 °C, in line with literature data [37]. The very shallow inflection at the T_g suggests a high degree of crystallinity, and in fact the melting-crystallization phenomenon is very evident. In the first heating scan, the melting event is observable at approx. 220 °C (see data of T_{m1} in Table 3), in line with the melting of the α crystalline phase of PA6, while the endothermic event in the second heating scan shows a shoulder at lower temperatures, associated with the melting of the γ crystalline phase at 214 °C. The melting temperature in the first heating scan slightly decreases with an increase in both the mold temperature, i.e., passing from 145 °C to 175 °C, and in the catalysts' concentrations, i.e., passing from L to H. Although a decrease in T_m may be due to an increase in the residual monomer, this is likely not the reason in this case, given that the residual monomer concentration is always very low (<2 %) and does not follow a specific trend with the composition or the mold temperature (see Table 4).

Conversely, the decrease in T_m may be caused by an increase in

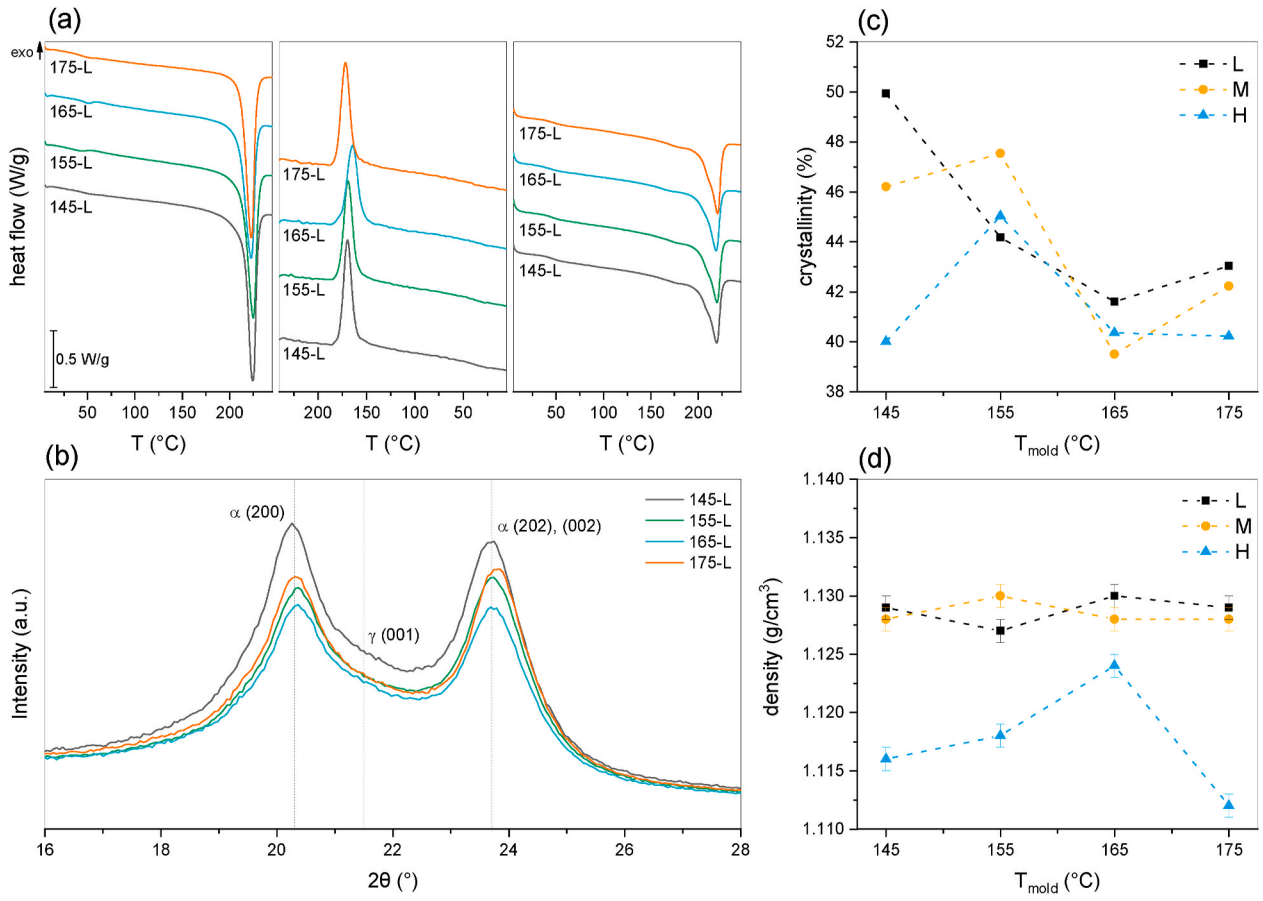

Fig. 2. (a) Representative DSC thermograms (first heating, cooling, and second heating scans) of some selected samples, i.e., 145-L, 155-L, 165-L, and 175-L; (b) XRD diffractograms of some selected samples, i.e., 145-L, 155-L, 165-L, and 175-L; (c) degree of crystallinity as a function of the composition and the mold temperature, calculated via DSC; (d) pycnometric density of all the prepared samples, as a function of the composition and the mold temperature.

Table 2
Crystalline fraction estimations via XRD analysis with area ratio. and profile fitting.

Sample	χ_{XRD} (%) Area ratio	χ_{XRD} (%) Profile fitting
145-L	34.07	56.49
155-L	31.93	53.68
165-L	29.86	48.76
175-H	31.42	54.22

Table 3
Main results of the DSC tests on all the prepared samples.

Sample	T_{m1} (°C)	ΔH_{m1} (J/g)	χ (%)	T_c (°C)	ΔH_c (J/g)	T_{m2} (°C)	ΔH_{m2} (J/g)
145-L	222.4	114.8	50.0	171.0	61.3	218.4	65.8
145-M	221.7	106.3	46.2	164.2	56.8	216.6	60.7
145-H	219.9	92.0	40.0	163.8	57.4	217.7	59.8
155-L	223.2	101.6	44.2	170.2	62.5	218.8	68.6
155-M	221.8	109.3	47.5	170.8	65.8	219.2	68.5
155-H	221.9	103.6	45.0	173.6	63.9	219.6	68.1
165-L	220.8	95.7	41.6	165.6	57.2	217.7	60.1
165-M	219.2	90.9	39.5	159.1	57.2	217.1	58.1
165-H	217.4	92.8	40.4	158.5	56.2	215.5	58.5
175-L	220.2	99.0	43.0	173.6	62.4	218.9	65.9
175-M	218.5	97.1	42.2	170.4	60.0	217.8	64.4
175-H	218.6	92.5	40.2	167.3	56.5	217.3	63.5

$T_{m1}, \Delta H_{m1}$ = melting temperature and enthalpy (first heating scan); χ = degree of crystallinity (first heating scan); $T_c, \Delta H_c$ = crystallization temperature and enthalpy (cooling scan); $T_{m2}, \Delta H_{m2}$ = melting temperature and enthalpy (second heating scan).

crosslinking/branching, well known to be promoted both by a higher polymerization temperature and a high activator and initiator concentration [20,37,38]. Branching can decrease the melting temperature in two ways, namely by promoting an increase in the γ phase at the expense of the α phase, and by favoring crystal imperfections, thereby decreasing the energy required for the melting event [39]. Given that the γ phase is not seen increasing considerably with an increase in the mold temperature, as explained later (see XRD results in Fig. 2c), the decrease in T_m is likely caused by a decrease in crystal perfection due to side reactions, branching, and crosslinking. This was indeed expected, since the higher the concentration of catalysts, the faster the polymerization rate and the monomer depletion, the shorter the polymer chains and the broader the molecular weight distribution [37,38]. Branching may be caused by the active amide anions on the polymer chain attacking the nearby chains rather than other monomer units [37,40]. Moreover, the probability of a difunctional activator, such as C20P, causing branched and crosslinked materials considerably increases at higher polymerization temperatures [37]. To try to measure the molecular weight, an attempt was made to dissolve the produced polymer in concentrated formic acid and sulfuric acid, as suggested in the literature [24,38,41–43], in order to measure the intrinsic viscosity via an Ubbelohde viscometer. However, full dissolution could never be achieved for any of the prepared samples, while swelling was always observed (Fig. S3). This, aside of preventing us from measuring the intrinsic viscosity, made us infer that all our samples were, to a certain extent, branched/crosslinked.

The same phenomena decreasing T_m are likely also responsible for a

Table 4
Main results of the TGA tests on all the prepared samples and conversion degree according to the water extraction method.

Sample	$T_{1\%}$ (°C)	$T_{3\%}$ (°C)	$T_{5\%}$ (°C)	T_{onset} (°C)	T_{d1} (°C)	T_{d2} (°C)	$m_{R,700}$ (wt%)	$m_{L,250}$ (wt%)	CD_{TGA} (%)	CD_w (%)
145-L	287.5	313.0	325.4	387.8	351.3	457.8*	0.25	0.53	99.5	99.4
145-M	216.3	300.5	312.5	376.9	337.8	441.7*	0.04	1.34	98.7	99.2
145-H	273.5	298.0	309.3	336.6	369.5*	389.3	0.00	0.49	99.5	99.2
155-L	265.8	308.0	323.8	383.7	357.2	451.5*	0.13	1.35	98.6	99.5
155-M	264.5	301.8	314.1	338.2	362.7*	389.7	0.00	0.78	99.2	99.2
155-H	221.1	293.9	307.0	317.6	340.7*	430.2	0.00	0.79	99.2	98.8
165-L	273.1	299.1	312.3	330.2	360.0*	452.8	0.00	0.45	99.6	99.1
165-M	269.0	298.2	312.6	328.2	352.3*	436.7	0.21	0.64	99.4	98.8
165-H	265.6	285.8	297.4	328.2	357.8*	373.7	0.09	0.53	99.5	99.5
175-L	264.2	292.0	305.7	327.1	360.0	448.2*	0.00	0.81	99.2	99.4
175-M	246.7	293.9	308.6	330.3	356.7*	428.0	0.39	1.04	99.0	99.3
175-H	259.7	293.6	307.9	334.7	355.0*	379.71	0.00	0.61	99.4	99.2

*$T_{1\%}$, $T_{3\%}$, $T_{5\%}$, = temperatures at a mass loss of 1 wt%, 3 wt%, or 5 wt%; T_{onset} = onset degradation temperature; T_{d1} = degradation temperature (1st DTG peak); T_{d2} = degradation temperature (2nd DTG peak); * indicates the most intense peak between T_{d1} and T_{d2}; $m_{L,250}$ = mass loss at 250 °C, corresponding to unreacted CL; $m_{R,700}$ = residual mass at 700 °C; CD_{TGA} = conversion degree according to TGA results, calculated as 100-$m_{L,250}$.*

decrease in the degree of crystallinity. As shown in Table 3 and Fig. 2c, χ generally decreases with an increase in the mold temperature and the catalysts concentration, although the effect of the catalysts concentration is more clearly visible at low mold temperatures. In any case, the crystallinity degree is quite high for all the prepared samples, being comprised between 40 and 50 %. The effect of polymerization temperature on the crystallinity degree is well known. The equilibrium degree of crystallinity is lower at higher polymerization temperatures due to the increased thermal motion of the polymer chains, and the balance between crystallization and polymerization is shifted towards the latter [18,44,45]. The same is true for a higher catalysts concentration, which also favors polymerization over crystallization. In fact, the highest crystallinity degree is found for the sample 145-L and is equal to 50.0 %. However, if the effect of the catalysts' concentration is very clear for the samples polymerized at lower temperatures, with 145-L being the most crystalline (50.0 %) and 145-H the least crystalline (40.0 %), the contribution of the composition to the crystallinity is more nuanced when the polymerization temperature increases. This implies that, for mold temperatures above 155 °C and for the type and fraction of catalysts considered in this work, a higher mold temperature will accelerate the polymerization and suppress crystallization, also with a low catalysts concentration.

To better understand the role of temperature in regulating microstructure and crystallinity, the samples with "L" composition were subjected to XRD. An example 2D WAXS image collected on sample 165L is reported in Fig. S4. Two strong diffraction rings are present, indexed as the (200) and (002)/(202) reflections of the PA6 α−polymorph. The resulting integrated 1D profile diffractograms for all the samples are shown in Fig. 2c. The peaks at 20.3° and 23.7° are associated with the thermodynamically stable α crystalline phase, and specifically to the diffraction planes (200) and (202)–(002), respectively. As described in previous works, this phase is associated with the formation of spherulites and other high-order superstructures and with high mechanical properties [44]. Conversely, only a very weak signal is present at 21.5°, associated with the less stable γ crystalline phase. This means that the selected polymerization temperatures are effective in inhibiting the formation of this phase, unlike what has been described in other works [37].

The resulting crystalline fractions obtained with the two different methodologies are reported in Table 2. While both results series seem to indicate the same qualitative trend, the profile fitting produces significantly higher values. It should be noted that both approaches are sensible to their specific numerical configurations, i.e., the number of profile points used for background fitting in the case of the area ratio method, and in the average nanocrystalline domain sizes for the amorphous signal in the case of profile modeling. For this reason, both results shall be taken as semi-quantitative, although profile fitting should be considered more robust. It can be observed that the results obtained with the profile fitting modeling are in good agreement with those obtained in DSC for the "L" compositions.

The generally lower crystallinity of the samples with an H composition (Fig. 2a) is also reflected in a lower gravimetric density. As reported in Fig. 2d, the density of the H samples is systematically lower than that of the other samples, while there is no appreciable difference between the density of the samples with compositions M and L. However, the lower density of the H samples may also derive from trapped air and nitrogen bubbles during reins transfer. In fact, the fast polymerization kinetics and the consequent rapid increase in viscosity of the H samples hinder the refill of liquid into the mold during resin transfer and promote the trapping of air bubbles into the polymerizing mass [23]. Moreover, the higher viscosity of the H composition forces injection with slightly higher pressure, which can create turbulence inside the mold, also conducive to gas incorporation. Conversely, it is unlikely that any residual CL might be a source of voids from trapped gas, as the boiling temperature of CL is 270.8 °C at 1 atm [46]. Although the temperature inside the mold rises because of the reaction exotherm, no temperature above 5 °C from the set mold temperature has ever been reported, making it extremely improbable that caprolactam would boil under the processing conditions utilized in this study.

TGA tests were performed to assess the thermal stability of the prepared samples. The TGA thermograms of some selected compositions are reported in Fig. 3, while all the main results of the TGA tests are shown in Table 4. The complete set of the TGA thermograms can be seen in the Supplementary Materials (Fig. S5). All samples present a very high thermal stability, with $T_{1\%}$ always located well above 200 °C and $T_{1\%}$ almost always above 300 °C. An increase in the catalysts' concentration and the polymerization temperature slightly anticipates the beginning of the thermal degradation, that is, the values of $T_{1\%}$, $T_{3\%}$, $T_{5\%}$, and T_{onset} decrease of 10–20 °C by passing from L to H and from 145 °C to 175 °C. In fact, the sample 145-L is the most thermally stable. Values of T_{onset} above 250 °C suggest a higher degree of conversion, which was calculated as the residual mass at 250 °C and reported in Table 4 as CD_{TGA}. Indeed, the mass loss at 250 °C is always below 150 °C, suggesting that polymerization occurs for all prepared samples with a yield higher than 98.5 %, in line or sometimes slightly higher than what is generally found in the literature (96–98 %) [24,36]. These values, in good agreement with those evaluated through water extraction (CD_w, Table 4), confirms the possibility to obtain high polymerization yields also with the lower catalysts concentration and at the lowest polymerization temperatures adopted in this study (i.e., the composition 145-L).

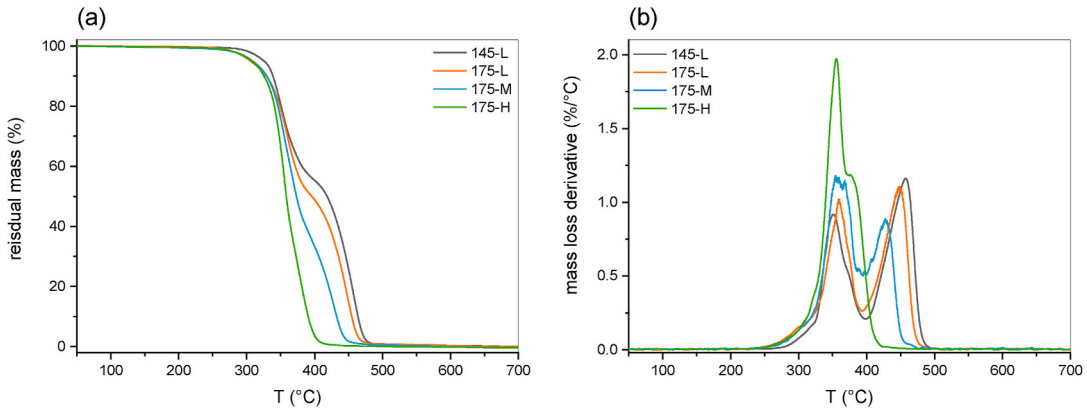

Fig. 3. Selected TGA thermograms of some representative compositions, i.e., 145-L, 175-L, 175-M, and 175-H. Residual mass (a) and mass loss derivative (DTG) (b) as a function of temperature.

Observing the DTG plot (Fig. 3b), the two degradation peaks suggest a thermal degradation in two subsequent steps. The first degradation peak is always located in the range of 340–375 °C, while the second peak shifts towards lower temperatures with an increase in the polymerization temperature, from 460 °C of the sample 145-L to 370 °C of 165-H. The intensity balance between the two peaks is shifted towards the first with a higher mold temperature and a higher catalysts concentration, which is evident by comparing the DTG thermograms of 145-L (black) and 175-H (green) in Fig. 3b. This two-stage degradation was also observed by other authors [12,24,44,47–49], but the results were seldom commented, and an explanation has never been provided. Although a proper measurement of the extent of molecular weight, branching, and crosslinking could not performed and is outside the scope of this work, this behavior observed in TGA may be associated to a bimodal distribution of the molecular weight and is compatible with the assumption that an increase in the catalysts concentration and the polymerization temperature accelerate the polymerization and multiply the number of growing chains, which causes a lower average molecular weight and shifts the degradation towards the first, low temperature peak.

Some selected samples were also studied via dynamic mechanical analysis, to gain information on the glass transition region. The results of

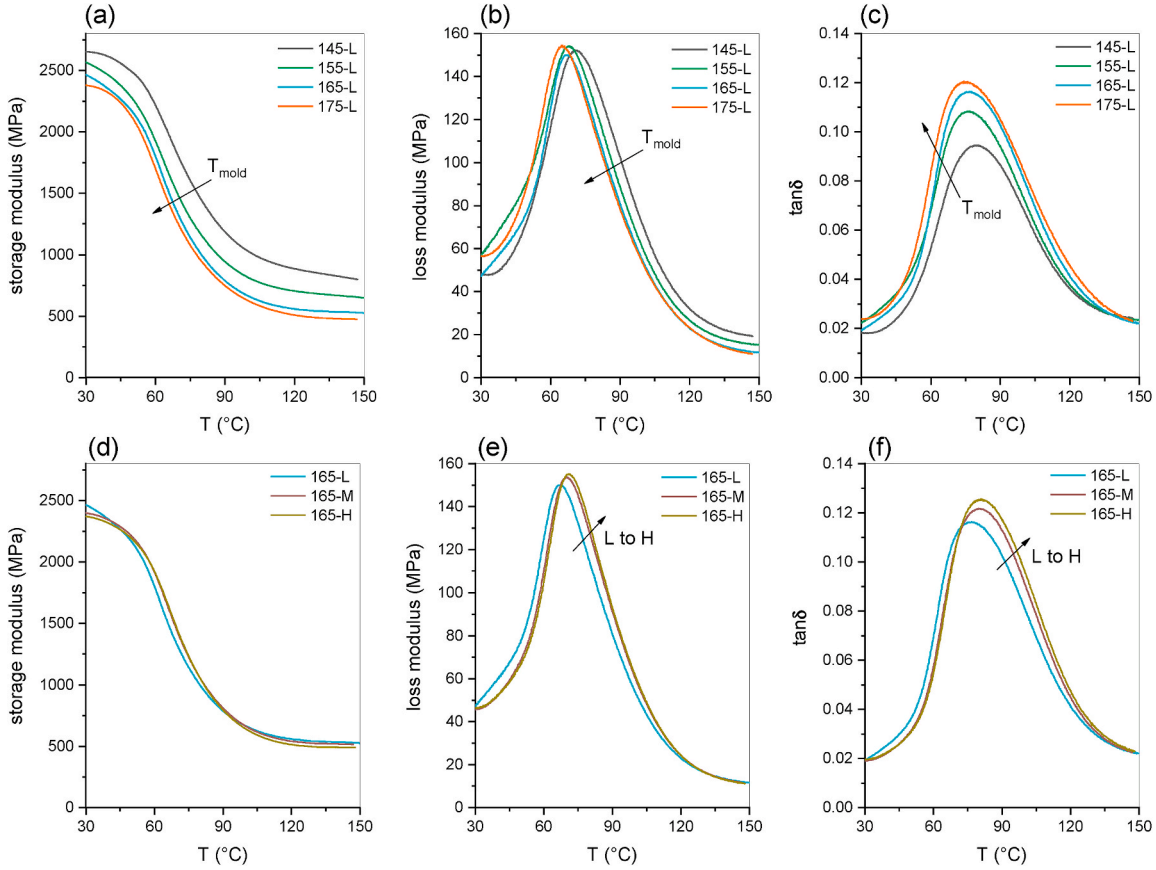

Fig. 4. DMTA thermograms of some representative compositions. (a–c) Effect of mold temperature: storage modulus, loss modulus, and tanδ as a function of temperature for the samples 145-L, 155-L, 165-L, and 175-L. (d-f) Effect of the catalyst concentration: storage modulus, loss modulus, and tanδ as a function of temperature for the samples 165-L, 165-M, and 165-H.

the DMTA tests are reported in Fig. 4 and Table 5. The main purpose of this test was to detect any possible major trends in the T_g and in other viscoelastic parameters. Hence, the test focused on some selected samples and was performed on only one specimen per sample. The authors are well aware that the DMTA tests may be affected by significant errors, but we believe that such data give a quantitative understanding of the qualitative trends seen in Fig. 4 and can therefore still be useful for the reader.

Fig. 4 shows the DMTA thermograms (E', E'', and $tan\ \delta$) of some selected compositions, i.e., al the L-samples at different polymerization temperatures (Fig. 4a–c) and the 165-samples at different catalysts concentrations (Fig. 4d–f). The value of E' are generally higher for lower polymerization temperatures (Fig. 4a), probably due to the higher crystallinity degree. All DMTA thermograms show a single, very evident relaxation between 40 °C and 90 °C, which can be associated with the glass transition (the "α-transition"), corresponding to a strong decrease in E' and to peaks in E'' and $tan\ \delta$. The location of the T_g, in line with the values reported in the literature for PA6, is an additional sign of a high conversion degree [50].

The peak of E'', associated with the T_g, shifts towards lower temperatures with an increase in the mold temperature (Fig. 4b–Table 5). This could be associated with a higher degree of crystallinity and, consequently, the increased fraction of amorphous phase constrained by the nearby crystalline domains. An increase in T_g is also observed by increasing the catalysts' concentration (Fig. 4e–Table 5), likely due to the increased density of branching and crosslinking points. The peaks of $tan\ \delta$ (Fig. 4c–f) also shift to lower temperature by increasing the polymerization temperature (Fig. 4c) and to higher temperatures by increasing the catalysts concentration (Fig. 4f), following the same trend of E''.

Finally, the characterization of the mechanical properties was performed through tensile tests, whose results, presented in Fig. 5a-e, evidence remarkable differences in the tensile behavior across the various compositions. Some samples show a brittle fracture immediately after yielding or in some cases even before it, while some other compositions fail after an extended plastic deformation zone.

The elastic modulus generally decreases with increasing mold temperature and is affected by the catalysts' concentration only at the lowest T_{mold}, thus following quite closely the degree of crystallinity reported in Fig. 2c. The values of E range between 3.4 GPa of the sample 145-L and 2.7 GPa of the sample 165-H, in good agreement with what has been reported in the literature [23,24,41]. The UTS also generally decreases with the polymerization temperature and, while it is higher for L compositions, it is lower for M compositions, with the H compositions fitting in between them. The only exception is for the samples polymerized at 175 °C, for which the composition M outperforms the other samples, similarly to what happens for the elastic modulus. In any case, the measured UTS values range between 68 and 80 MPa and are similar or higher than those reported in the literature for similar compositions and mold temperatures [21,23,24]. Finally, the strain at break generally increases with the mold temperature, which is particularly evident for the L-samples. The only exception is the sample 175-L, which shows the lowest ε_b across all the tested samples (11 %). The highest ductility is instead shown by the sample 165-L, which presents an average ε_b of 48 %. This remarkable difference between samples 165-L and 175-L may be due to the slightly higher degree of crystallinity and larger presence of production defects and bubbles of the sample 175-L, for which several specimens broke in correspondence of a defect, but more investigation is needed to fully clarify this point. The ductility of the fracture of the sample 165-L is also evident from the SEM micrograph of its fracture surface (Fig. 5b), which shows characteristic cup-cone morphology and evident signs of polymer stretching. This morphology is remarkably different from that of a sample presenting a brittle fracture, such as specimen 145-H, also shown in Fig. 5b.

Table 5
Main results of the DMA tests on some representative compositions. The measurements were performed on one specimen per sample.

Sample	E' (30 °C) (MPa)	E' (150 °C) (MPa)	$T_{g,E''}$ (°C)
145-L	2650	790	70.8
155-L	2565	648	67.8
165-L	2463	526	66.5
165-M	2397	516	70.2
165-H	2369	489	71.2
175-L	2377	471	64.8

To dig deeper into the understanding of the remarkable impact of the polymerization temperature and the catalysts' concentration on the mechanical properties, an in-depth statistical analysis was performed, to build empirical models for the target yields. First, a correlation map was produced to easily visualize the possible correlations between all the involved variables [51]. Besides the two chosen factors (T_{mold} and C) and the three target yields (E, UTS, and ε_b), also the degree of crystallinity calculated in DSC (χ) was included as a variable. The resulting correlation map can be observed in Fig. 6, which reports the Pearson's r index for each couple of variables. The closer the r value to the extremes −1 and 1, the higher the linear correlation between the two considered variables. Generally, two variables are considered significantly correlated when r is higher than 0.4 or lower than −0.4 [51,52]. The diagonal of the correlation map represents the correlation of each variable with itself (by definition $r = 1$, visually represented by a straight line with slope 1). Moreover, of course T_{mold} and C are not correlated (r close to 0). It is interesting to observe that E, UTS, and χ are inversely correlated with T_{mold}, which confirms the observations reported in Fig. 5, while C seems to be significantly linearly correlated only with χ. Moreover, E and χ show a relatively strong linear correlation ($r = 0.62$), in good agreement with the previous discussion. Finally, ε_b does not seem to be significantly linearly correlated with any of the other considered variables.

After the correlation matrix, a response surface analysis was performed for each of the target yields. The response surface analysis on the elastic modulus starting from a full quadratic model resulted in the regression model presented in Eq. (6),

$$E = 4101.95 - 704.18 \cdot T_{mold} - 191.84 \cdot C + 94.53 \cdot {T_{mold}}^2 + 63.68 \cdot T_{mold} \cdot C. \quad (6)$$

From the full ANOVA results of the model for E, reported in Table S1 and Table S2, it can be observed that all the terms selected in the model are statistically significant ($p < 0.05$), while those that are not significant, such as C^2, were not reported. Moreover, the model itself is significant, while the lack of fit [53] of this model compared to the full quadratic model (Eq. (5)) is not significant ($p > 0.05$), which means that the model reported in Eq. (6) with only the selected terms can fit the experimental data as precisely as the full quadratic model. The residuals of the model are normally distributed ($p < 0.05$). The adjusted R^2, which is always comprised between 0 and 1 and reflects how closely the model can fit the experimental results of the model is 0.523 ($R^2 = 1$ for a perfect fit), which denotes a certain ability of the model to fit the experimental results.

The graphical representation of the model for E is illustrated in Fig. 7a, which reports the contour plot of the model. This visual representation is useful to illustrate how E is affected by T_{mold} and C. As already mentioned while discussing the experimental results, it is clear that E is maximum for a low temperature and catalysts concentration and it decreases with increasing T_{mold} , while the concentration of catalysts seems to affect E only at low mold temperatures. In other words, if at 145 °C E steeply decreases while passing from L, to M, to H, at higher temperatures the variation in E while moving vertically on the plot is minimal. Indeed, the parameter C is not significant in the ANOVA analysis of E (Table S1) (it was kept to preserve the model's hierarchy),

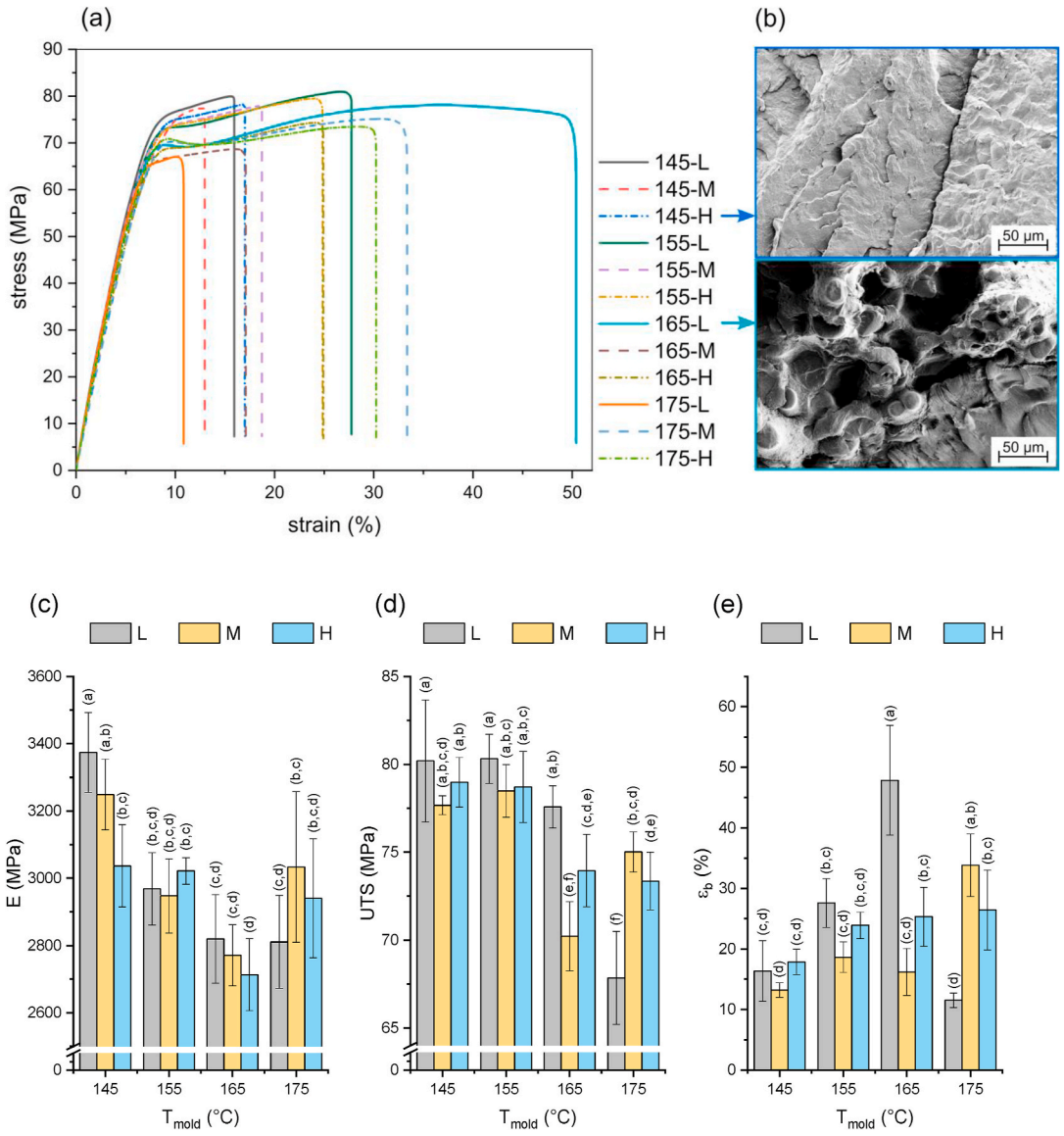

Fig. 5. Main results of the tensile tests on the prepared samples. (a) Representative tensile stress-strain curves of all the prepared compositions; (b) tensile fracture surface of 145-H (top), as an example of brittle fracture, and 165-L (bottom), as an example of ductile fracture; (c–e) elastic modulus, ultimate tensile strength, and strain at break as a function of the composition and the mold temperature. Letters in brackets represent the results of Tukey's HSD test, performed after the two-way ANOVA (same letter means no significant difference, i.e., $p > 0.05$).

while the interaction parameter T_{mold}: C is.

The RSM is a powerful statistical technique used to model and analyze the relationship between input variables (factors) and output variables (responses). While the primary objective of RSM is often to identify the optimal combination of input variable levels that yield the desired response value (maximizing E in this case), there are instances where prioritizing the stability of the response variable becomes more advantageous. This scenario arises when slight variations in the input variables, which are inevitable due to inherent process variability or measurement errors, cannot be tolerated due to the need for consistent and predictable outputs. In such cases, the response surface plot can be leveraged to identify regions where the slope is relatively shallow or where saddle points exist. These regions are characterized by minimal changes in the output variable, even when subjected to small fluctuations in the input variables. Consequently, operating within these regions ensures that the process maintains a stable output, minimizing the risk of significant deviations caused by slight variations in the input variables. This approach becomes particularly beneficial in applications where product quality, safety, or consistency is paramount, such as in industrial and manufacturing processes. In this specific case, while the maximum elastic modulus is measured at low mold temperatures and low catalysts concentrations, it may be more advantageous to produce PA6 materials at intermediate to high mold temperatures, because in these regions the influence of small variations in the input parameters causes a small variation in the output.

The response surface analysis on *UTS* starting from a full quadratic model resulted in the regression model presented in Eq. (7),

$$UTS = 87.4655 + 4.5771 \cdot T_{mold} - 2.5548 \cdot C + 0.9930 \cdot T_{mold} \cdot C. \quad (7)$$

From the full ANOVA results of the model for *UTS*, reported in Table S3 and Table S4, it can be observed that all the terms selected in the model are statistically significant ($p < 0.05$) and the model itself is significant, while the lack of fit of this model compared to the full quadratic model (Eq. (5)) is not significant ($p > 0.05$), which means that the model reported in Eq. (7) with only the selected terms can fit the experimental data as precisely as the full quadratic model. The residuals of the model are normally distributed ($p < 0.05$) and the adjusted R^2 of the model is 0.504, which denotes a certain ability of the model to fit the

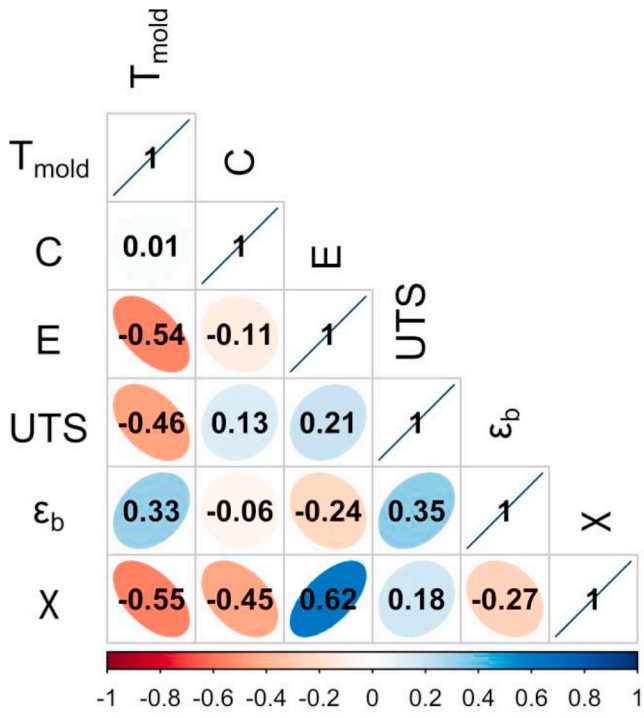

Fig. 6. Correlation map between all the considered factors (T_{mold} and C) and yields (E, UTS, and ε_b). The degree of crystallinity measured in DSC (χ) was also added to the correlation map. The color and the shape of the ellipsis are associated with Pearson's r coefficient, also indicated in the map. (For interpretation of the references to color in this figure legend, the reader is referred to the Web version of this article.)

experimental results.

The graphical representation of the model for *UTS* is illustrated in Fig. 7b, which reports the contour plot of the model. Also in this case, this visual representation is useful to illustrate how *UTS* is affected by T_{mold} and C, and *UTS* is maximum for a low temperature and catalysts concentration and it decreases with increasing T_{mold} , while the concentration of catalysts affects UTS to a lesser extent. Indeed, as in the case of E, the parameter C is not significant in the ANOVA analysis of *UTS* (Table S3) (it was kept to preserve the model's hierarchy), while the interaction parameter T_{mold}: C is.

Finally, the response surface analysis ε_b starting from a full quadratic model resulted in the regression model presented in Eq. (8),

$$\varepsilon_b = 0.3812 + 18.2171 \cdot T_{mold} - 3.0652 \cdot T_{mold}^2. \quad (8)$$

From the full ANOVA results of the model for ε_b, reported in Table S5 and Table S6, it can be observed that all the terms selected in the model are statistically significant ($p < 0.05$) and the model itself is significant, while the lack of fit of this model compared to the full quadratic model (Eq. (5)) is not significant ($p > 0.05$), which means that the model reported in Eq. (8) with only the selected terms can fit the experimental data as precisely as the full quadratic model. This in particular means that the terms containing the dependence on the catalysts concentration are not necessary to increase the capability of the model to fit the experimental data, when only the quadratic terms are considered. This is evident also from the graphical representation of the model for ε_b is illustrated in Fig. 7c, in which the dependence on C is totally absent. However, the experimental data suggest that a certain dependence on C may be present, at least at intermediate mold temperatures. Indeed, greater ductility manifested by the composition 165-L, compared to that of 165-M and 165-H, may suggest that a low catalysts concentration may be beneficial to increase ε_b, due to a probable increase in the average molecular weight. Based on these physical considerations, and on the very low adjusted R^2 of the model (i.e., 0.170) and the not normally distributed residuals ($p = 0.0196$), it was decided to try to fit the experimental data with a model described by an equation of order 3, i.e., by adding terms such as T_{mold}^3, C^3, $T_{mold}^2 \cdot C$, and $C^2 \cdot T_{mold}$. Then, after an ANOVA analysis, only the significant terms were kept. The response surface analysis of ε_b obtained in this way resulted in the regression model presented in Eq. (9),

$$\varepsilon_b = -40.051 + 64.190 \cdot T_{mold} + 20.389 \cdot C - 12.796 \cdot T_{mold}^2 - 23.252 \cdot T_{mold} \cdot C + 4.923 \cdot T_{mold}^2 \cdot C. \quad (9)$$

From the full ANOVA results of this new model for ε_b, reported in Table S7 and Table S8, it can be observed that all the terms selected in the model are statistically significant ($p < 0.05$) and the model itself is significant, while the lack of fit of this model compared to the full cubic model is not significant ($p > 0.05$). The residuals of the model are this time normally distributed ($p < 0.05$). The adjusted R^2 of this model is 0.314, still quite far from 1, but higher than that of the previous model with only quadratic terms. Additionally, from the contour plot reported in Fig. 7d, it is evident that this model can capture the interestingly high strain at break obtained at low catalysts concentrations and intermediate mold temperatures, likely resulting from a low crystallinity, a moderate branching, and a relatively high molecular weight.

4. Conclusions

This work presents a systematic investigation that unveils the intricate interplay between mold temperature and catalysts concentration on the microstructural and thermo-mechanical properties of anionic polyamide 6 (aPA6) prepared via in-situ polymerization. The novelty lies in the comprehensive evaluation of these two critical processing parameters, which profoundly influence the polymerization kinetics, degree of conversion, microstructure, and ultimately, the mechanical performance of the aPA6 material. Through a combined experimental and statistical approach, key correlations between the processing conditions and the resulting material properties have been established, providing valuable insights for optimizing the processing of this interesting reactive thermoplastic polymer.

The mold temperature and catalysts concentration significantly affect the degree of crystallinity, with higher temperatures and higher concentrations reducing crystallinity due to the promotion of polymerization over crystallization. These processing parameters also impact the thermal stability and degradation behavior of aPA6, as higher temperatures and higher catalysts concentrations slightly anticipate the onset of thermal degradation. The elastic modulus and ultimate tensile strength are primarily governed by the mold temperature, with lower temperatures resulting in higher values due to the increased crystallinity. The catalysts concentration has a lesser effect, primarily influencing these properties at lower mold temperatures. Interestingly, the strain at break exhibits a more complex dependence on both processing parameters, with intermediate mold temperatures and lower catalysts concentrations promoting higher ductility, possibly due to an optimal balance between crystallinity, branching, and molecular weight.

Statistical models have been developed to quantitatively describe the relationships between the processing parameters and the mechanical properties, enabling the prediction and optimization of the aPA6 performance within the studied variable ranges. The insights gained offer a framework for tailoring the microstructure and mechanical properties of aPA6 through precise control of mold temperature and catalysts concentration. This knowledge is particularly valuable for liquid composite molding techniques, such as thermoplastic resin transfer molding, where precise control over the polymerization kinetics and resulting material properties is crucial.

In summary, this systematic investigation provides a comprehensive understanding of the intricate relationships between processing conditions and material properties in anionic polyamide 6, offering valuable guidance for optimizing the manufacturing of high-performance

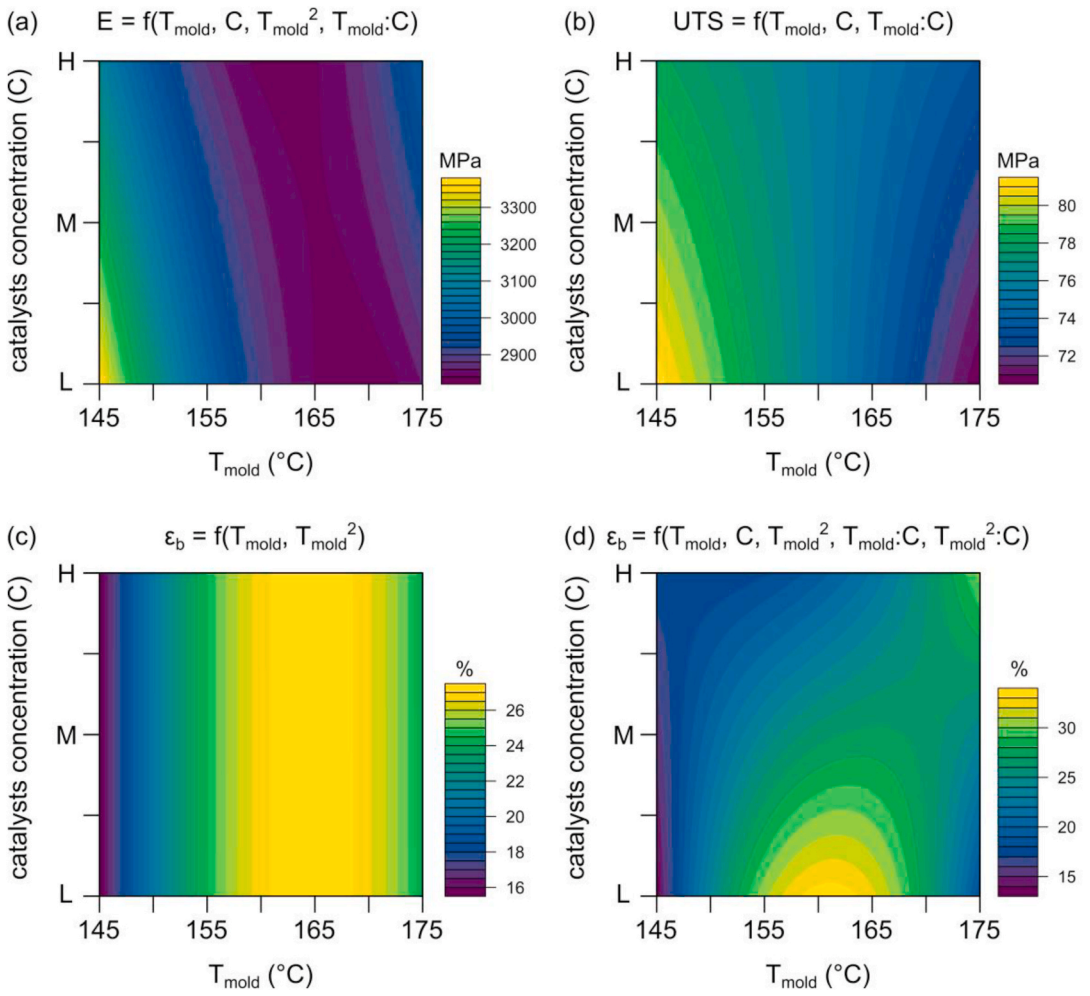

Fig. 7. Contour plots of the empirical models resulting from the statistical analysis of the mechanical tests. (a) Contour plot of the elastic modulus (***E***) as a function of the mold temperature (T_{mold}) and catalysts concentration (***C***); (b) Contour plot of the tensile strength (***UTS***) as a function of T_{mold} and ***C***; (c) Contour plot of the strain at break (ε_b) as a function of T_{mold} and ***C***, considering only the quadratic terms; (d) Contour plot of the strain at break (ε_b) as a function of T_{mold} and ***C***, considering also the third order terms.

thermoplastic composites based on this promising reactive matrix system. Future works will focus on the exploitation of this knowledge for the production of continuous fiber thermoplastic composites with various kinds of reinforcements and on the investigation of the fiber/matrix interfacial interaction.

CRediT authorship contribution statement

Giulia Fredi: Writing – review & editing, Writing – original draft, Visualization, Supervision, Methodology, Investigation, Formal analysis, Data curation, Conceptualization. **Lorenzo Broggio:** Writing – review & editing, Visualization, Investigation. **Martino Valentini:** Writing – review & editing, Visualization, Investigation, Formal analysis. **Mauro Bortolotti:** Writing – review & editing, Investigation, Formal analysis. **Daniele Rigotti:** Writing – review & editing, Resources, Methodology. **Andrea Dorigato:** Writing – review & editing, Supervision, Resources. **Alessandro Pegoretti:** Writing – review & editing, Supervision, Funding acquisition.

Declaration of competing interest

The authors declare the following financial interests/personal relationships which may be considered as potential competing interests.

Giulia Fredi reports financial support was provided by European Commission. If there are other authors, they declare that they have no known competing financial interests or personal relationships that could have appeared to influence the work reported in this paper.

Data availability

Data will be made available on request.

Acknowledgments

L. Brüggemann GmbH & Co. KG is kindly acknowledged for providing the monomer and catalysts. Mr. Davide Perin is gratefully acknowledged for his support to SEM observations. Mr. Alfredo Casagranda and Ms. Claudia Gavazza are gratefully acknowledged for their support to the experimental activities. The work has been produced with the co-funding of the European Union, FSE-REACT-EU, PON Research and Innovation (Action IV.6 - Green) 2014–2020 DM1062/2021.

Appendix A. Supplementary data

Supplementary data to this article can be found online at https://doi.org/10.1016/j.polymer.2024.127562.

References

[1] M. Valente, I. Rossitti, I. Biblioteca, M. Sambucci, Thermoplastic composite materials approach for more circular components: from monomer to in situ polymerization, a review, Journal of Composites Science 6 (5) (2022) 132, https://doi.org/10.3390/jcs6050132.

[2] K. van Rijswijk, H.E.N. Bersee, Reactive processing of textile fiber-reinforced thermoplastic composites – an overview, Compos. Appl. Sci. Manuf. 38 (3) (2007) 666–681, https://doi.org/10.1016/j.compositesa.2006.05.007.

[3] A. Belkhiri, N. Virgilio, E. Santanach-Carreras, J. Esvan, V. Nassiet, H. Welemane, O. De Almeida, F. Chabert, Influence of silane interfacial chemistry on the curing process of anionic Polyamide 6 in glass reinforced composites, Colloids Surf. A Physicochem. Eng. Asp. 676 (2023) 132183, https://doi.org/10.1016/j.colsurfa.2023.132183.

[4] L. Sun, M. Cao, F. Xiao, J. Xu, Y. Chen, POSS functionalized graphene oxide nanosheets with multiple reaction sites improve the friction and wear properties of polyamide 6, Tribol. Int. 154 (2021) 106747, https://doi.org/10.1016/j.triboint.2020.106747.

[5] T. Ageyeva, I. Sibikin, J.G. Kovacs, A review of thermoplastic resin transfer molding: process modeling and simulation, Polymers 11 (10) (2019) 1555, https://doi.org/10.3390/polym11101555.

[6] R.T. Durai Prabhakaran, Are reactive thermoplastic polymers suitable for future wind turbine composite materials blades? Mech. Adv. Mater. Struct. 21 (3) (2013) 213–221, https://doi.org/10.1080/15376494.2013.834090.

[7] Y. Qin, J. Summerscales, J. Graham-Jones, M. Meng, R. Pemberton, Monomer selection for in situ polymerization infusion manufacture of natural-fiber reinforced thermoplastic-matrix marine composites, Polymers 12 (12) (2020) 2928, https://doi.org/10.3390/polym12122928.

[8] T. Ageyeva, I. Sibikin, J. Karger-Kocsis, Polymers and related composites via anionic ring-opening polymerization of lactams: recent developments and future trends, Polymers 10 (4) (2018) 357, https://doi.org/10.3390/polym10040357.

[9] I. Sibikin, J. Karger-Kocsis, Toward industrial use of anionically activated lactam polymers: past, present and future, Advanced Industrial and Engineering Polymer Research 1 (1) (2018) 48–60, https://doi.org/10.1016/j.aiepr.2018.06.003.

[10] P. Dubois, O. Coulembier, J.-M. Raquez, Handbook of Ring-Opening Polymerization, WILEY-VCH Verlag GmbH & Co. KGaA, Weinheim, Germany, 2009.

[11] J. Karger-Kocsis, T. Bárány, Single-polymer composites (SPCs): status and future trends, Compos. Sci. Technol. 92 (2014) 77–94, https://doi.org/10.1016/j.compscitech.2013.12.006.

[12] Y. Gong, A. Liu, G. Yang, Polyamide single polymer composites prepared via in situ anionic polymerization of ε-caprolactam, Compos. Appl. Sci. Manuf. 41 (8) (2010) 1006–1011, https://doi.org/10.1016/j.compositesa.2010.04.006.

[13] Y. Gong, G. Yang, All-polyamide composites prepared by resin transfer molding, J. Mater. Sci. 45 (19) (2010) 5237–5243, https://doi.org/10.1007/s10853-010-4565-6.

[14] N. Dencheva, Z. Denchev, A.S. Pouzada, A.S. Sampaio, A.M. Rocha, Structure–properties relationship in single polymer composites based on polyamide 6 prepared by in-mold anionic polymerization, J. Mater. Sci. 48 (20) (2013) 7260–7273, https://doi.org/10.1007/s10853-013-7546-8.

[15] S. Dinparast Tohidi, Z.Z. Denchev, A.M. Rocha, N.V. Dencheva, B. Engesser, A. S. Pouzada, Mechano-morphological studies of polyamide 6 based single polymer laminate composites prepared by different reactive processing techniques, Polym. Test. 79 (2019) 106017, https://doi.org/10.1016/j.polymertesting.2019.106017.

[16] L. Song, X. Wang, P. Xie, Y. Ding, K. Dang, W. Yang, Dissolution window in in situ polymerization preparation of polyamide single-polymer composites, Polym. Eng. Sci. 61 (6) (2021) 1662–1672, https://doi.org/10.1002/pen.25690.

[17] S. Jalali, G. Greco, D. Rigotti, A. Dorigato, H. Mirbaha, G. Fredi, M. Bertolla, S. Guerra, T. Battistini, A. Dal Moro, A. Pegoretti, N.M. Pugno, Micromechanical model for single-polymer composites and experimental validation on self-reinforced PA6-based composites, Composites Part A 180 (2024) 108042, https://doi.org/10.1016/j.compositesa.2024.108042.

[18] J. Humphry, N. Wolter, N. Yang, L.J. Vandi, R. Truss, D.J. Martin, M.T. Heitzmann, Process modelling in Anionically Polymerised Polyamide-6 (APA6) for the in situ polymerisation of composite matrices, Compos. Commun. 8 (2018) 111–114, https://doi.org/10.1016/j.coco.2017.12.011.

[19] J. Humphry, N. Yang, L.J. Vandi, B.V. Hernandez, D.J. Martin, M.T. Heitzmann, Isothermal differential scanning calorimetry analysis of the anionic polymerisation of polyamide-6: separation by dual asymmetric Gaussians, Mater. Today Commun. 25 (2020) 101473, https://doi.org/10.1016/j.mtcomm.2020.101473.

[20] K. van Rijswijk, H.E.N. Bersee, W.F. Jager, S.J. Picken, Optimisation of anionic polyamide-6 for vacuum infusion of thermoplastic composites: choice of activator and initiator, Compos. Appl. Sci. Manuf. 37 (6) (2006) 949–956, https://doi.org/10.1016/j.compositesa.2005.01.023.

[21] M. Wilhelm, R. Wendel, M. Aust, P. Rosenberg, F. Henning, Compensation of water influence on anionic polymerization of ε-caprolactam: 1. Chemistry and experiments, Journal of Composites Science 4 (1) (2020) 7, https://doi.org/10.3390/jcs4010007.

[22] R. Wendel, P. Rosenberg, M. Wilhelm, F. Henning, Anionic polymerization of ε-caprolactam under the influence of water: 2. Kinetic model, Journal of Composites Science 4 (1) (2020) 8, https://doi.org/10.3390/jcs4010008.

[23] K. van Rijswijk, H.E.N. Bersee, A. Beukers, S.J. Picken, A.A. van Geenen, Optimisation of anionic polyamide-6 for vacuum infusion of thermoplastic composites: influence of polymerisation temperature on matrix properties, Polym. Test. 25 (3) (2006) 392–404, https://doi.org/10.1016/j.polymertesting.2005.11.008.

[24] J. Lagarinhos, L. Santos, J. Oliveira, Effect of catalyst and activator on properties of polyamide 6 prepared by thermoplastic resin transfer molding technology, J. Mater. Eng. Perform. 31 (9) (2022) 7098–7103, https://doi.org/10.1007/s11665-022-07044-4.

[25] Z. Kovács, Á. Pomázi, A. Toldy, The flame retardancy of polyamide 6—prepared by in situ polymerisation of ε-caprolactam—for T-RTM applications, Polym. Degrad. Stabil. 195 (2022) 109797, https://doi.org/10.1016/j.polymdegradstab.2021.109797.

[26] O.V. Semperger, A. Suplicz, The effect of the parameters of T-RTM on the properties of polyamide 6 prepared by in situ polymerization, Materials 13 (1) (2019) 4, https://doi.org/10.3390/ma13010004.

[27] Z. Osváth, A. Szőke, S. Pásztor, G. Szarka, L.B. Závoczki, B. Iván, Post-polymerization heat effect in the production of polyamide 6 by bulk quasiliving anionic ring-opening polymerization of ε-caprolactam with industrial components: a green processing technique, Processes 8 (7) (2020) 856, https://doi.org/10.3390/pr8070856.

[28] J. Filik, A.W. Ashton, P.C.Y. Chang, P.A. Chater, S.J. Day, M. Drakopoulos, M. W. Gerring, M.L. Hart, O.V. Magdysyuk, S. Michalik, A. Smith, C.C. Tang, N. J. Terrill, M.T. Wharmby, H. Wilhelm, Processing two-dimensional X-ray diffraction and small-angle scattering data in DAWN 2, J. Appl. Crystallogr. 50 (Pt 3) (2017) 959–966, https://doi.org/10.1107/S1600576717004708.

[29] D.R. Holmes, C.W. Bunn, D.J. Smith, The crystal structure of polycaproamide: nylon 6, J. Polym. Sci. 17 (1955) 159–177, https://doi.org/10.1002/pol.1955.120178401.

[30] M. Bortolotti, L. Lutterotti, I. Lonardelli, ReX: a computer program for structural analysis using powder diffraction data, J. Appl. Crystallogr. 42 (3) (2009) 538–539, https://doi.org/10.1107/s0021889809008309.

[31] L. Lutterotti, R. Campostrini, S. Gialanella, R. Di Maggio, Microstructural characterisation of amorphous and nanocrystalline structures through diffraction methods, J. Metastable Nanocryst. Mater. 8 (2000) 657–664. https://doi.org/10.4028/www.scientific.net/JMNM.8.657.

[32] R-Cran. https://cran.r-project.org/.

[33] R. Rosenthal, R. R, Essentials of Behavioral Research: Methods and Data Analysis, McGraw Hill, Boston, MA, USA, 2008.

[34] G.E.P. Box, K.B. Wilson, On the experimental attainment of optimum conditions, J. Roy. Stat. Soc. B 13 (1951) 1–45, https://doi.org/10.1111/j.2517-6161.1951.tb00067.x.

[35] D.C. Montgomery, G.C. Runger, Applied Statistics and Probability for Engineers, seventh ed., John Wiley & Sons, Inc., Hoboken, NJ, USA, 2018.

[36] S. Russo, A. Imperato, A. Mariani, F. Parod, The fast activation of ε-caprolactam polymerization in quasiadiabatic conditions, Macromol. Chem. Phys. 196 (1995) 3297–3303.

[37] L. Ricco, S. Russo, G. Orefice, F. Riva, Anionic poly(ε-caprolactam): relationships among conditions of synthesis, chain regularity, reticular order, and polymorphism, Macromolecules 32 (1999) 7726–7731, https://doi.org/10.1021/ma9909004.

[38] K. Oh, H. Kim, Y. Seo, Effect of diamine addition on structural features and physical properties of polyamide 6 synthesized by anionic ring-opening polymerization of epsilon-caprolactam, ACS Omega 4 (17) (2019) 17117–17124, https://doi.org/10.1021/acsomega.9b01342.

[39] P.J. Flory, Thermodynamics of crystallization in high polymers. IV. A theory of crystalline states and fusion in polymers, copolymers, and their mixtures with diluents, J. Chem. Phys. 17 (3) (1949) 223–240, https://doi.org/10.1063/1.1747230.

[40] K. Udipi, R.S. Davé, R.L. Kruse, L.R. Stebbins, Polyamides from lactams via anionic ring-opening polymerization: 1. Chemistry and some recent findings, Polymer 38 (4) (1997) 927–938, https://doi.org/10.1016/S0032-3861(96)00566-6.

[41] N. Barhoumi, A. Maazouz, M. Jaziri, R. Abdelhedi, Polyamide from lactams by reactive rotational molding via anionic ring-opening polymerization: optimization of processing parameters, Express Polym. Lett. 7 (1) (2013) 76–87, https://doi.org/10.3144/expresspolymlett.2013.7.

[42] Z. Kan, M.-b. Yang, W. Yang, Z.-y. Liu, B.-h. Xie, Investigation on the reactive processing of textile-ramie fiber reinforced anionic polyamide-6 composites, Compos. Sci. Technol. 110 (2015) 188–195, https://doi.org/10.1016/j.compscitech.2015.01.023.

[43] S.D. Tohidi, A.M. Rocha, N.V. Dencheva, Z. Denchev, Microstructural-mechanical properties relationship in single polymer laminate composites based on polyamide 6, Compos. B Eng. 153 (2018) 315–324, https://doi.org/10.1016/j.compositesb.2018.08.106.

[44] C. Vicard, O. De Almeida, A. Cantarel, G. Bernhart, Experimental study of polymerization and crystallization kinetics of polyamide 6 obtained by anionic ring opening polymerization of ε-caprolactam, Polymer 132 (2017) 88–97, https://doi.org/10.1016/j.polymer.2017.10.039.

[45] C. Vicard, O. De Almeida, A. Cantarel, G. Bernhart, Modeling of the polymerization and crystallization kinetic coupling of polyamide 6 synthesized from ε-caprolactam, Polymer 180 (2019) 121681, https://doi.org/10.1016/j.polymer.2019.121681.

[46] Pubchem - National library of medicine. https://pubchem.ncbi.nlm.nih.gov/compound/7768.

[47] Z. Gao, R. Zhao, S. Cai, X. Ning, An applicability study on various methods for determining the monomer conversion rate of polyamide 6, J. Appl. Polym. Sci. (2024), https://doi.org/10.1002/app.55487.

[48] B. Wu, K. Zhu, F. Wang, X. Wen, M. Li, Y. Yang, J. Yang, Development of PA6/GO microspheres with good processability for SLS 3D printing, Polym. Eng. Sci. 62 (5) (2022) 1700–1709, https://doi.org/10.1002/pen.25957.

[49] O.V. Semperger, A. Suplicz, The degradation during recycling of polyamide 6 produced by anionic ring-opening polymerization of epsilon-caprolactam, Sci. Rep. 13 (1) (2023) 17130, https://doi.org/10.1038/s41598-023-44314-0.
[50] H. Shi, L. Xia, Z. Guo, A. Sun, H. Wang, Z. Kan, Manufacture and performance of textile-ramie fiber reinforced anionic polyamide 6 composites, Fibers Polym. 20 (8) (2019) 1705–1715, https://doi.org/10.1007/s12221-019-8968-y.
[51] A. Bucciarelli, C. Reddy Chandraiahgari, A. Adami, V. Mulloni, L. Lorenzelli, Precise dot inkjet printing thought multifactorial statistical optimization of the piezoelectric actuator waveform, Flexible and Printed Electronics 5 (4) (2020) 045002, https://doi.org/10.1088/2058-8585/abbb7e.
[52] H. Akoglu, User's guide to correlation coefficients, Turk J Emerg Med 18 (3) (2018) 91–93, https://doi.org/10.1016/j.tjem.2018.08.001.
[53] D.L. Mohr, W.J. Wilson, R.J. Freund, Statistical Methods, fourth ed., Elsevier Inc., Cambridge, MA, USA, 2022.